

Single-Particle Tracking To Probe the Local Environment in Ice-Templated Crosslinked Colloidal Assemblies

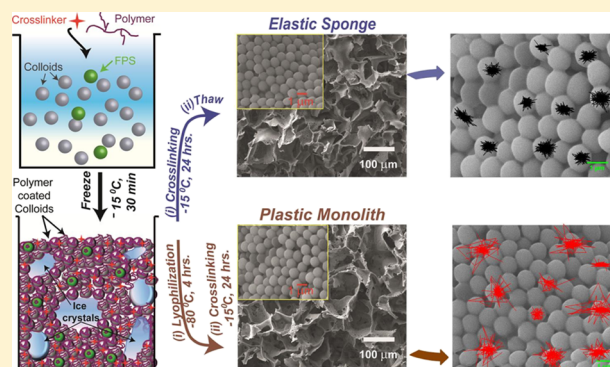
Karthika Suresh,[†] Dharmendar Kumar Sharma,^{‡,||} Ramya Chulliyil,[‡] Ketan Dinkar Sarode,^{§,⊥} V. Ravi Kumar,[§] Arindam Chowdhury,^{*,‡,||} and Guruswamy Kumaraswamy^{*,†,||}

[†]J-101, Polymers and Advanced Materials Laboratory, Complex Fluids and Polymer Engineering, Polymer Science and Engineering Division, and [§]Chemical Engineering Division, CSIR-National Chemical Laboratory, Pune 411008, Maharashtra, India

[‡]Department of Chemistry, Indian Institute of Technology Bombay, Powai, Mumbai 400076, Maharashtra, India

S Supporting Information

ABSTRACT: We use single-particle tracking to investigate colloidal dynamics in hybrid assemblies comprising colloids enmeshed in a crosslinked polymer network. These assemblies are prepared using ice templating and are macroporous monolithic structures. We investigate microstructure-property relations in assemblies that appear chemically identical but show qualitatively different mechanical response. Specifically, we contrast elastic assemblies that can recover from large compressive deformations with plastic assemblies that fail on being compressed. Particle tracking provides insights into the microstructural differences that underlie the different mechanical response of elastic and plastic assemblies. Since colloidal motions in these assemblies are sluggish, particle tracking is especially sensitive to imaging artifacts such as stage drift. We demonstrate that the use of wavelet transforms applied to trajectories of probe particles from fluorescence microscopy eliminates stage drift, allowing a spatial resolution of about 2 nm. In elastic and plastic scaffolds, probe particles are surrounded by other particles—thus, their motion is caged. We present mean square displacement and van Hove distributions for particle motions and demonstrate that plastic assemblies are characterized by significantly larger spatial heterogeneity when compared with the elastic sponges. In elastic assemblies, particle diffusivities are peaked around a mean value, whereas in plastic assemblies, there is a wide distribution of diffusivities with no clear peak. Both elastic and plastic assemblies show a frequency independent solid modulus from particle tracking microrheology. Here too, there is a much wider distribution of modulus values for plastic scaffolds as compared to elastic, in contrast to bulk rheological measurements where both assemblies exhibit a similar response. We interpret our results in terms of the spatial distribution of crosslinks in the polymer mesh in the colloidal assemblies.



1. INTRODUCTION

Colloidal assemblies are technologically important materials with implications for nanoscale electronics,¹ energy conversion/storage devices,² photonic and plasmonic devices,³ drug and gene delivery systems,⁴ diagnostic systems,⁵ as well as for catalysis.⁶ However, the fragile mechanical response of colloidal assemblies limits their use.⁷ Therefore, there is intense research focused on understanding the structural underpinnings of failure in colloidal assemblies and into leveraging this understanding to prepare mechanically robust colloidal assemblies.^{8–11} Recently, we have demonstrated the preparation of hybrid colloid–polymer assemblies that exhibit remarkable elastic recovery from large compressive strains exceeding 90%, despite an inorganic particle content of 90% by weight.¹² These macroporous assemblies were prepared by ice-templating and comprise colloids held in a crosslinked polymer mesh to form centimeter-sized monoliths. We have shown that such elastic assemblies are obtained for several different colloids (including polystyrene latex, silica colloids, hydroxyapatite,

etc.), for different polymers (including polyethylenimine (PEI) of different molecular weights, gelatin, etc.) and for different crosslinking chemistries (using glutaraldehyde or diepoxide crosslinkers). Thus, the exceptional mechanical properties of the spongelike assembly are not a consequence of the chemical composition of the constituents. Rather, they can be attributed to the inorganic–organic hybrid microstructure that is formed using the ice-templating protocol, viz., freezing an aqueous dispersion of colloids, polymer, and crosslinker, and allowing crosslinking to happen in situ after the water has frozen. This chemistry-independence has allowed us to select suitable functional materials to prepare elastic colloidal sponges for applications ranging from flexible supercapacitors¹³ to tissue engineering scaffolds¹² and separation media.¹⁴

Received: December 1, 2017

Revised: March 15, 2018

Published: March 20, 2018

We have recently investigated the microstructure that develops in these ice-templated hybrids, to understand its relation to the observed elastic mechanical response.¹⁵ We have shown that the mechanical response is sensitive to the preparation protocol employed to prepare the assemblies. For example, if the ice crystals formed by freezing the colloidal dispersion are removed by lyophilization, so that crosslinking happens in the absence of ice, the resultant monoliths are plastic, viz., they fail on compressing even to small strains. Surprisingly, the overall chemical composition of such plastic monoliths is indistinguishable from the elastic sponges. Both are macroporous and are characterized by the same pore size distribution. They are both characterized by the same organic content, the same polymer to crosslinker ratio, and the same average crosslink density. Therefore, the stark differences between the mechanical response of elastic and plastic scaffolds must arise from subtle local variations in their microstructure. Previously, we have reported atomic force microscopy (AFM) investigations of the local structure of elastic and plastic scaffolds.¹⁵ AFM results suggest that elastic sponges are characterized by relatively uniform crosslink density, while there are large spatial variations in the crosslink density in plastic monoliths. Thus, even when the average crosslink density is similar for elastic sponges and plastic monoliths, these subtle local differences in crosslinking result in widely different response to mechanical compression. Therefore, developing sensitive probes that can interrogate local microstructure hold promise for insights into material properties and material failure. Specifically, such probes can provide independent confirmation of the local microstructural differences between elastic sponges and plastic monoliths.

Probing the dynamics of colloids embedded in the monoliths provides information about the local environment around the colloid. For colloids held in a crosslinked polymer mesh, we anticipate that colloidal motions are highly restricted, rendering microscopy observations of such motions highly challenging. Particle tracking, using optical microscopy is routinely employed to investigate the dynamics of Brownian colloids in low viscosity Newtonian liquids. In contrast, the motion of colloids embedded in monoliths is sluggish, rendering microscopy challenging. The use of direct microscopic observation however has significant advantages and has been used to quantify motions in dense colloidal systems to access local, micron-scale dynamics. For example, Weeks et al. employed confocal microscopy to study dynamical changes near the jamming transition of a concentrated colloidal glass.¹⁶ They could identify caging of particle motions in colloidal glasses and reported the observation of dynamic heterogeneities and structural relaxation phenomena near the colloidal glass transition. The microscopic structure of shear thickening or shear thinning colloidal suspensions has also been investigated using microscopy,¹⁷ where the thermal motion of several thousand particles are tracked with high spatio-temporal resolution. Such techniques are being used to provide insights into cellular processes in biology,^{18,19} local plasticization in polymer matrices,²⁰ adsorption–desorption dynamics,²¹ local heterogeneity in clay suspensions, polymeric thickener solutions, food gels, and so forth.^{22–26}

Investigating the dynamics of sluggish colloidal systems, where particle motion is highly restricted, requires high resolution optics that are stable over long imaging durations. Remarkable advances have been made in spatial resolution in single-molecule microscopy.^{27,28} Of specific interest to us are

laser epifluorescence techniques that limit the excitation volume to a very narrow depth, thus reducing the contribution of out of focus, background light.²⁹ The spatial resolution that one can achieve using these methods is strongly dependent on the signal to background ratio (SBR). Harnessing these methods to problems in colloid science would make it possible to investigate systems where displacements are too small to be probed using conventional imaging tools. Dekker et al. have shown that non diffraction limited particles imaged using 40 \times magnification and with $SBR \geq 20$ could be tracked with a spatial resolution of ≈ 10 nm.³⁰ However, when imaging colloidal particles (instead of single molecules), the sluggish nature of the systems requires imaging over long durations, typically several minutes or more. In such experiments, unless an extremely stable microscopy setup is used, one has to guard against artifacts in single-particle tracking data. The most common problem is sample stage or focus drift which may arise because of a variety of reasons, including vibrations, acoustic noise, and thermal drift.^{31,32} When particle motions are themselves small (\sim few nanometers) with respect to the external factors mentioned, even stage drift of a few tens of nanometers could result in erroneous apparent particle motion. To reduce mechanical drift, microscopes are typically mounted on air-cushioned optical benches. In addition, several post acquisition techniques have been utilized to correct for stage drift. These rely either on the use of fiducial markers in the sample³³ or marker-less methods such as template matching.³⁴ Bloëß et al.³⁵ reported optical imaging of single fluorescent molecules with a reproducibility of 3.4 nm in lateral position,³⁵ attained by mechanical drift correction by observing the position of a spatial reference in the sample. Carter et al.³⁶ further improved the resolution of single-molecule experiments by eliminating drift by referencing with a fiducial mark on the microscope coverslip.³⁶ In their experiments, drift was corrected through a feedback coupled piezoelectric stage and gave a stability of 0.17 nm for tens of seconds. However, the use of external markers with brightness that is very different from the particles of interest could result in camera pixel saturation, and further, the marker position with respect to the sample cannot be predetermined. Finally, template-matching techniques rely on distinct image features and a consistent background structure that are not always available. Therefore, the use of fiducial markers or template matching to eliminate stage drift cannot be practiced in all experimental situations.

If the number of particles (N) in a frame is large, researchers have suggested subtraction of the average tracer center-of-mass motion from the particle trajectory. However, this approach introduces an error in the mean square displacement (MSD) of the order of $1/N$, which is therefore advisable once when the number of tracers in a frame is much greater than 10.³⁷ Crocker et al.^{37,38} have described another protocol to eliminate stage drift, where they calculate the correlated motion of two particles in a frame along their line of centers. They used regression techniques to fit this motion to a model and used this to calculate the two point microrheology.^{37,38} However, application of this process to frames that contain several particles is rather tedious.

Here, we demonstrate the use of wavelet transforms to eliminate stage drift from single-particle tracking data collected on fluorescent micrometer polystyrene beads which form a part of the network. Wavelet transforms have been used in particle tracking experiments for multiscale detection of particle motions, denoising, 3D deconvolution of fluorescence micro-

graphs, and for extending the depth of field.³⁹ We report a facile method that uses commonly available software tools and allows for the elimination of stage drift from microscopy data to obtain tracer localization down to few nanometers. We then utilize this method to examine colloidal dynamics in elastic sponges and plastic monoliths and demonstrate differences in the spatial variation of crosslinking density in elastic and plastic scaffolds.

2. MATERIALS AND METHODS

2.1. Materials. “Angstrom sphere” spherical silica particles ($1\ \mu\text{m}$) were obtained from Richen Industries (Hong Kong). Monodisperse $1.08\ \mu\text{m}$ (SD = $0.04\ \mu\text{m}$) fluorescent polystyrene spherical particles (PS-FluoGreen-1.0, ab/em: 492/519 nm, 2.5 wt %) were obtained from microParticles GmbH (Germany). Branched PEI (25 kDa), 1,4-butanediol diglycidyl ether and polyvinylpyrrolidone (PVP, MW—40 kDa) were obtained from Sigma-Aldrich. All materials were used as received. Glass coverslips (No. 1, Corning, USA) were used as the substrate in particle tracking experiments.

2.2. Methods. **2.2.1. General Protocol for the Synthesis of Self-Standing Monoliths from Colloidal Particles.** Silica particles (60 mg, $1\ \mu\text{m}$) and 2 mg of $1\ \mu\text{m}$ fluorescent PS (FPS) particles were dispersed in deionized water (overall particle concentration in the dispersion is 10 wt %). This dispersion was sonicated for 15 min followed by 5 min vortexing. To this aqueous dispersion was added 3 mg of PEI (30 μL of 100 mg/mL polymer stock solution) and was mixed by vortexing for 5 min. To this was added 10 mg of 1,4-butanediol diglycidyl ether followed by 3 min vortexing.

2.2.2. Preparation of Elastic Sponges. The aqueous dispersion was placed in a freezer maintained at $\approx -15\ ^\circ\text{C}$ for 24 h followed by thawing at room temperature.

2.2.3. Preparation of Plastic Monoliths. The aqueous dispersion was frozen for 30 min at $-15\ ^\circ\text{C}$ followed by lyophilization for 4 h at $-80\ ^\circ\text{C}$, to sublime the ice crystals. After removal of ice, the sample was maintained at $-15\ ^\circ\text{C}$ for 24 h to allow crosslinking. After crosslinking, both elastic and plastic scaffolds were washed thoroughly in water (Figure 1).

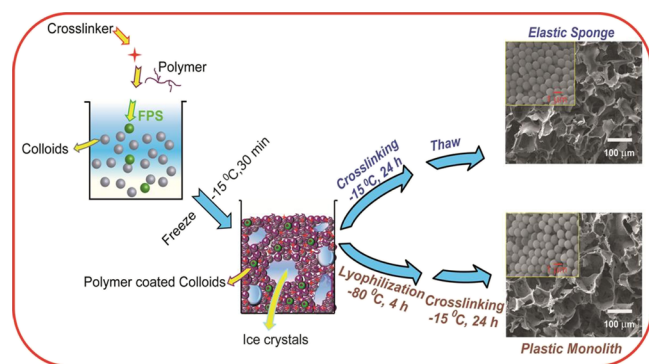


Figure 1. Protocol for the preparation of elastic sponge and plastic monolith. SEM morphology shows that both elastic and plastic scaffolds are macroporous, with hybrid pore walls comprising packed colloids held together by a crosslinked polymer mesh.

2.2.4. Preparation of the Reference Glassy Sample for Calibration of the Single-Particle Tracking Experiment. PS particles ($1\ \mu\text{m}$) were mixed with 4 wt % aqueous PVP solution. The uniformly mixed solution was drop-cast on a clean glass coverslip. The sample was annealed at $80\ ^\circ\text{C}$ for a day under vacuum. The annealed reference sample was placed inside a home-built humidifier mounted over the microscope stage and maintained at ambient temperature and pressure. Humidity in the enclosed chamber was controlled by regulating the Ar gas flow that was passed through water and then into the chamber. Temperature and humidity were maintained constant during all measurements. Glass coverslips were cleaned by first sonicating for 10 min in Piranha solution and then in 2 M NaOH,

followed by washing several times with Milli-Q water and with methanol. After drying by blowing N_2 gas, the coverslips were burned in an oxidizing flame to remove any fluorescent impurity on the coverslip.

2.2.5. Scanning Electron Microscopy. The sample morphology was imaged using a Quanta 200 3D scanning electron microscope (SEM). Thin slices were cut from the scaffolds using a surgical blade. These were mounted on SEM stubs and were coated by sputtering a thin layer of gold on their surface before imaging.

2.2.6. Particle Tracking. The fluorescent particles were imaged using a home-built epifluorescence microscope. A 488 nm cw diode-pumped solid-state laser (Laserglow, 50 mW) was passed through a circular polarizer and was focused onto the back focal plane of a $60\times$, 1.49 NA oil immersion objective (Nikon, Apo plan TIRF), so as to illuminate a circular area of the sample. Neutral density filters were used to control the excitation power. The light emitted by the sample was collected using the same objective lens and passed through a dichroic mirror. The emitted light was guided through a pin hole and filter wheel and impinged on a cooled ($-25\ ^\circ\text{C}$) interline CCD camera (DVC-1412AM). Time lapse movies were collected for 10 min at 1 Hz with an exposure time of 150 ms. Image data were collected as a movie using DVC View software. Subsequently, background subtraction and smoothing were performed using ImageJ software (NIH). After background subtraction, fluorescent particles appear as bright spots with the SBR of 20–35 (Supporting Information S1). To locate the spatial positions of these bright individual particles over time, we have used single-particle tracking program written in MATLAB 7.8. The program algorithm is based on the centroid method.²⁰ Here, we extract X and Y coordinates of the centroids of the bright spots and assign these as the particle center-of-mass position (algorithm details are in Supporting Information S2). Thus, particle coordinates are obtained for all frames of the movie and are used to extract the particle trajectories. We use wavelet transforms to eliminate artifacts during single-particle tracking. We describe the method used briefly in the Results section and in greater detail in the Supporting Information S2.

All measurements were performed at $23\ ^\circ\text{C}$ temperature and 60% relative humidity (RH). The RH was monitored using a RH probe positioned a few mm away from the sample. We maintain a constant temperature of $23\ ^\circ\text{C}$ using an ambient temperature control system. We constantly monitor the temperature during the experiment using a thermocouple connected to the microscope sample stage. The measurements were repeated several times to confirm their reproducibility.

3. RESULTS AND DISCUSSION

3.1. Using Wavelet Transforms to Filter out Stage Drift in Particle Tracking Experiments. We begin by using epifluorescence microscopy to investigate the reference sample. Individual $1\ \mu\text{m}$ fluorescent polystyrene beads embedded in a glassy PVP matrix appear as bright spots against a dark background (Figure S1a and SBRs of particles are shown in Figure S1b). Relative humidity is controlled to $<20\%$ during imaging experiments to prevent humidity-induced plasticization of the glassy matrix. Raw microscopy data suggest that the fluorescent polystyrene bead traverses over 100 nm in the PVP matrix over a time span of 10 min (Figure 2a, 2b). Such a large length scale motion of micron-sized colloids embedded in glassy matrices is physically unrealistic. Literature reports of microscope investigations of the motion of small molecules embedded in a glassy matrix suggest that these molecules are essentially frozen in the matrix, viz., motions, if any, are characterized by sub-nanometer length scales.²⁰ Therefore, the apparent trajectories of the $1\ \mu\text{m}$ latex particles, spanning over 100 nm, must arise from experimental artifacts.

We now discuss the origin for the observed drift in particle motion. It may be seen that widely separated fluorescent particles embedded in the glassy matrix show correlated motion

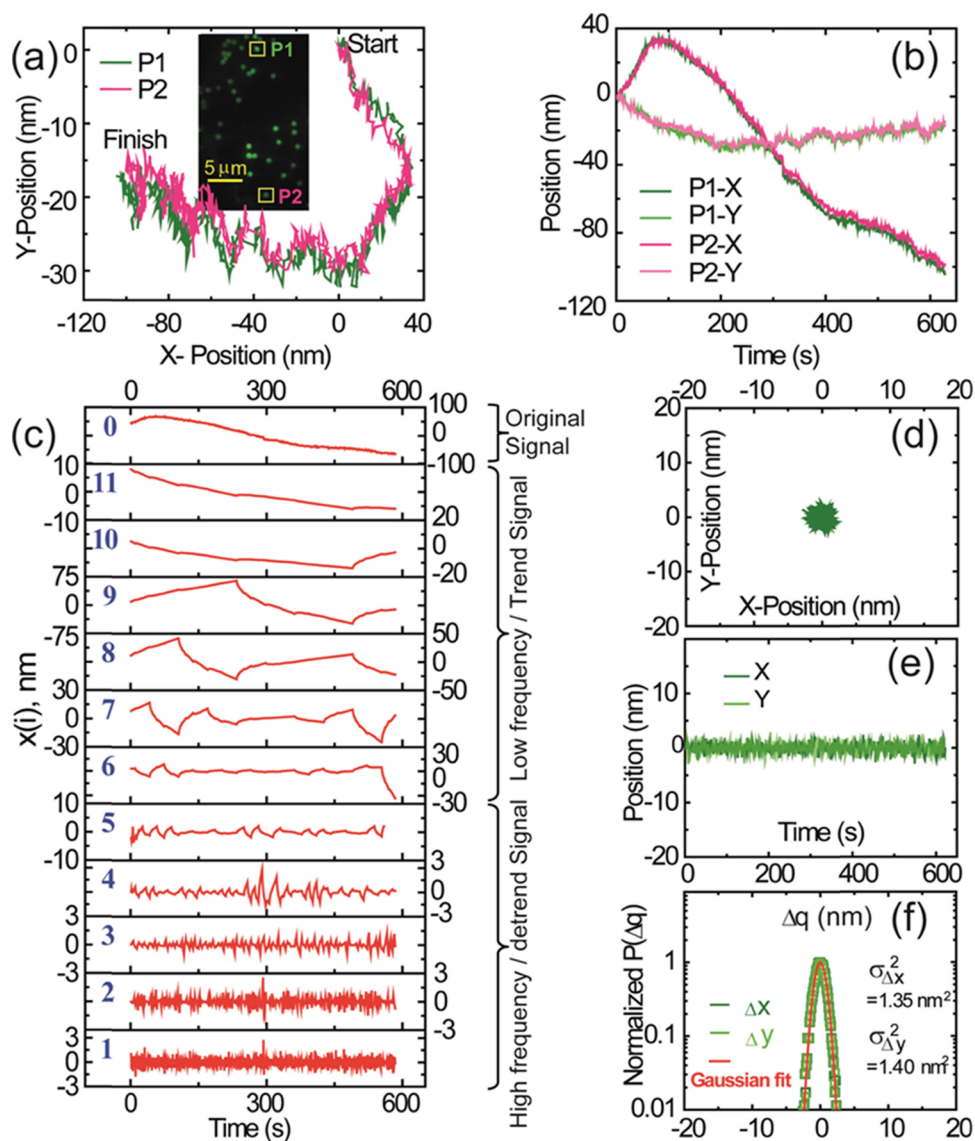


Figure 2. Fluorescence microscopy data from tracking of individual probe particles in reference glassy sample. (a) Trajectory of two FPS particles embedded in PVP glassy matrix. The inset shows a microscopy image. Note that the probe particles are readily resolved and are widely separated making it easy to track the motions of individual particles. (b) Trajectories shown in (a) are represented as the time-dependent motion of the two particles along arbitrary X and Y coordinates, with coordinate axes as defined in (a). (c) Wavelet transform studies of the X -component of the reference data showing scale-wise reconstruction, $X(i)$ ($i = 1, 2, \dots, 11$). $X(0)$ is the reconstructed lossless data and equivalent to the X -component. (d,e) The trajectory and time-dependent position along X and Y axes of a particle, after removal of stage drift. (f) Jump length distribution for particle “jumps” per frame along the X and Y axes. The jump distribution is well-fitted by a Gaussian, as shown.

(Figure S1c plots particle motion along an arbitrarily determined X -coordinate for three particles in the same image frame but separated by about $30 \mu\text{m}$). Such slow motion over long experimental timescales, of the order of 10 min, has been previously reported¹⁸ and has been attributed to stage drift. Stage drift can arise from vibrations (despite the use of vibration damping in our experiments), drift in the stepper motors used for sample positioning, temperature fluctuations (e.g., induced by environmental changes or variations in laser source intensity), and so forth. Stage drift represents a persistent experimental challenge when microscopy is used to track motion in samples over long timescales ($\sim\text{min}$). We now demonstrate how wavelet transforms can be used to deconvolute stage drift from particle Brownian motion in analysis of microscopy data.

Wavelet transforms can be used to deconvolute raw data into a series of time/frequency scales. Unlike the sine/cosine basis, mother functions used are wavelets with varying time/frequency properties that are compact.^{40–42} Thus, the convolution of the signal with the wavelets using wavelet transform convolutes the signal into frequency scales, that preserve temporal information in the signal and that help in monitoring events as they occur in time (detailed description of wavelet transform in Supporting Information S2). Therefore, it is advantageous to use wavelet transforms to eliminate effects of stage drift from microscopy data. We evaluated several different wavelet basis sets and observed that we were able to adequately represent the tracked signals using the Daubechies basis set.^{43,44} Daub4 wavelets are commonly used for analyzing spiky signals and can provide a good representation of the Brownian fluctuations in our data (see Supporting Information S2 for

criteria employed to select an appropriate wavelet basis set). Here, we present analysis of our data using code previously developed in our group for this purpose^{45–48}. However, such analysis can also be readily performed using several commercial analysis tools. We have confirmed that the results of analysis using commercial routines are consistent with that from our in-house codes (see [Supporting Information S2](#) for more details).

We define arbitrary XY coordinate axes for the motion of the polystyrene colloid in glassy PVP and plot motion along these coordinates from the raw microscopy data ([Figure 2b](#)). We then subject the X and Y motion to a wavelet transform to subtract the lateral drift in long-term time lapse imaging. The wavelet transform characterizes the different frequency components that are present in the original raw signal (mean removed) to obtain the wavelet scalogram shown in the frequency—time panels of [Figure 2c](#). From the lossless nature of the orthogonal wavelet transform using Daub4 wavelets, we obtain the raw signal $x(0, t) = \sum_{i=1}^{11} x(i, t)$ over the entire time period ($t = n\Delta t$, where Δt is the sampling interval and $n = 1, 2, \dots$ is the discretized data point index), in terms of the scalogram components ($i = 1, 2, \dots, 11$) shown in the panels of [Figure 2c](#). Components in higher scales represent the low frequency signal that tracks the stage drift, which is known as the trend signal. Lower scales represent the high frequency “noise” about the drift, referred to as the detrend signal. The scale-wise signal power is then given by $P(i) = \sum_t x(i, t)^2$. We observe that the power corresponding to scales (6–11) is significantly higher than those for scales 1–5 ([Supporting Information: Figure S2IV](#)). Therefore, the signal in scales 1–5 is masked by that in scales 6–11. We use this threshold in power to assign scales 6–11 as the trend signal and scales 1–5 as the detrend signal (also see [Supporting Information, Figure S2V](#)). Carrying out the inverse wavelet transform using the wavelet coefficients for scales $i = 1, 2, \dots, 5$ only unmask the fluctuating component which is now separated from the trend in scales 6–11 ([Figure S2VI](#)). In all the samples studied here, we observe that $i = 5$ corresponds to the threshold value in the power. This gives us further confidence in assigning $i = 6–11$ as the drift signal. This gives the reconstructed trend (see [Supporting Information, Figure S2VIa](#)) and detrend ([Figure S2VIb](#)) signal by inverse wavelet transform. This allows the elimination of correlations that exist in the motion of the particles in the same image frame ([Figure S2VII](#)). Thus, we have established that reconstructing the particle center-of-mass motion based on the detrend signal (using scales 1–5) eliminates stage drift in our particle tracking experiment ([Figure 2d,e](#)). Analysis with different colloidal samples showed similar trending and detrending behavior, and a generalized protocol could be obtained. Therefore, we could now subject every individual probe particle to a wavelet analysis. Thus, by analyzing the microscopy data, the excursions of the particles about its mean position could be calculated ([Figure 2d,e](#)). We also calculated the “jumps” made by the particle over the minimum time interval of 1 s, along the X and Y coordinates by using the formula, $\Delta q = (q_{i+t} - q_i)$, where q is X or Y coordinates and t is the step time ([Figure 2f](#)) and observed that the jump distributions (or van Hove distributions) along both X and Y coordinates are similar. We fitted the jump distributions to a Gaussian shape and note that they are characterized by a variance of $\approx 1.4 \text{ nm}^2$. Since we do not anticipate any measurable motion of these large colloidal particles in a glassy matrix, the data analysis determined the resolution limit of measurements to about $\pm 2.5 \text{ nm}$ which is

the width of the Gaussian at $P(\Delta q) = 10^{-2}$. We have also calculated jump distributions for the particles with a step sizes of 2 and 4 s (viz., excursions of the particles across 2 frames or 4 frames) and note that the width of the van Hove distributions are largely independent of the step size ([Figure S2VIII](#)). Additionally, we have examined the motion of probe particles at different local concentrations and have confirmed that the resolution from the van Hove distribution is independent of the probe particle concentration. We reiterate that to obtain this resolution, we require high SBRs of probes and elimination of artifacts using wavelet transforms.

3.2. Particle Motions in Elastic and Plastic Scaffolds.

Having established a protocol to obtain particle motions by eliminating stage drift, we now apply this to particle tracking data obtained from elastic and plastic scaffolds. Particle scaffolds are prepared by ice-templating a mixture of silica and FPS colloids¹⁵ ([Figure 1](#)). The scaffolds are macroporous, with $\approx 50 \mu\text{m}$ pores bounded by walls comprising colloids bound together in a crosslinked polymer mesh. We use a sparse concentration of fluorescent colloids of size matched with the silica particles. Only the fluorescent particles are visualized in the microscopic image, and as the FPSs are an integral part of the pore walls, tracking their motion provides us insights into how the pore wall microenvironment governs particle dynamics.

We first describe the results obtained from elastic scaffolds. We imaged and tracked multiple (at least 10) FPS particles in the same field of view and observed that particle motions are correlated, even for widely separated particles ([Figure S3I](#)). We attribute these correlated motions to stage drift and employ wavelet transforms, as described in the previous section to eliminate the low frequency correlated motion (see details in [Supporting Information S3](#)). [Figure 3a,b](#) shows the time-dependent trajectory of one representative particle and the time-dependent particle position along arbitrary XY coordinates, respectively. Using wavelet transform to eliminate the “trend” corresponding to scales 6–11, we obtain the noise which corresponds to position fluctuations because of thermal motion of the particle ([Figure 3c,e](#)). It is important to note that the observed fluctuations in position are significantly larger than those observed for the completely immobilized “frozen” reference sample (colloidal PS particle in the glassy matrix, compare [Figure 3c–e](#) with [Figure 2d–f](#)). Therefore, the motion observed for the colloidal particles in the scaffolds are above the resolution limit of our technique. Similarly, we analyze the raw tracking data (trajectory) from plastic scaffold for a representative FPS particle ([Figure 4a,b](#)) and use wavelet transforms to eliminate the drift ([Figure 4c–e](#)). Here too, we find that the thermal fluctuations of the FPS embedded in the walls of the plastic monolith are considerably higher than those for the immobilized (frozen) reference sample ([Figure 2d–f](#)) as well as that obtained for the elastic scaffolds ([Figure 3c–e](#)). From these trajectories, we obtain the MSD in both X and Y directions for probe particles in elastic and plastic scaffolds, and X and Y MSDs are found to be comparable for all particles ([Figures 3f](#) and [4f](#) respectively). We find that the MSD is linear in time for short lag times and subsequently plateaus over longer timescales, which is expected for particles embedded in these scaffolds.

To test the reliability of our deconvolution method using wavelet transforms, we have tracked and analyzed more than 100 probe FPS particles in both the elastic and plastic scaffolds. Particles are chosen from widely different spatial locations in

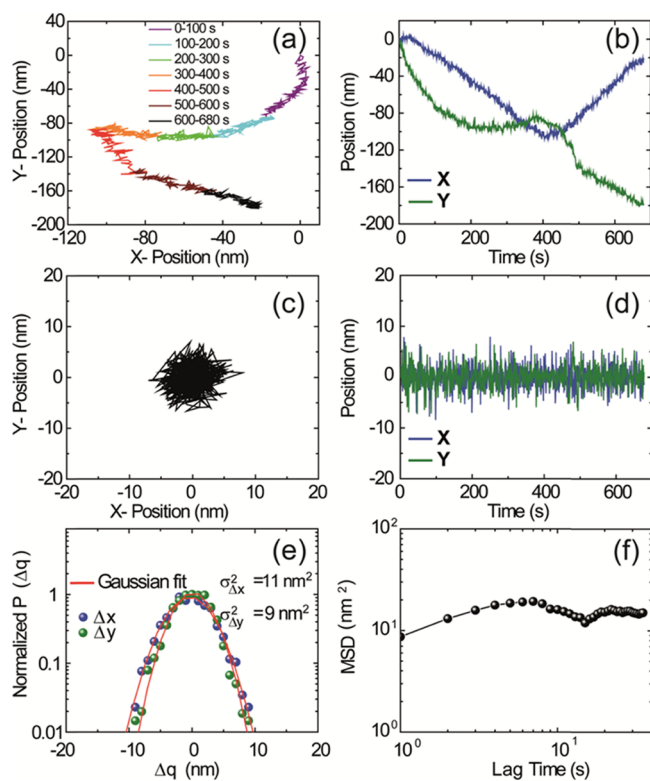


Figure 3. Microscopy investigation of elastic sponges. (a) Particle trajectory of a single probe particle from fluorescence microscopy. The trajectory is color-coded to show the timescale of motion. (b) Particle motion along X and Y coordinates (defined arbitrarily, as shown in (a)) as a function of time. (c,d) Trajectory and position of a particle after elimination of stage drift using wavelet transform. (e) van Hove jump distribution for a particle along X and Y coordinates, fit to a Gaussian form. (f) MSD for particle movement in the X – Y plane. We calculate MSD based on frames collected over about 10 min of imaging but restrict our interpretation to only the first 5% of the lag time, τ , to ensure statistical reliability.

each sample, over at least 10 independent samples. This allowed us to construct statistically reliable displacement jump distributions and MSD(τ) for each scaffold. Figure 5a,b shows the probability jump distributions (van Hove self-correlation functions) of all the FPS particles undergoing a specific distance (Δq , $q = X, Y$) within a minimum time interval of 1 s, for the elastic and plastic scaffolds, respectively, and compared to that of the reference sample where colloidal motions are frozen. It is clear that the motions that we observe in these samples are significantly larger than the instrumental resolution, set by the fluctuations of FPS beads, immobilized probe in a glassy matrix. Further, we can readily observe that the jump distribution spans a much wider range for plastic particles, when compared with the elastic particles. Because the variance of the jump distribution is related to the short time particle diffusivity,⁴⁹ we fit each jump distribution to a Gaussian function to extract the distribution of diffusivity for probe particles in the elastic and plastic scaffolds (Figure 5c). We also note that jump distributions for elastic particles from different spatial locations and different samples are relatively similar, with diffusion coefficients spanning from ~ 1.6 to ~ 40 nm^2/s and peaking at ≈ 4 nm^2/s (Figure 5c). In contrast, there is considerably more heterogeneity in the diffusivity of particles embedded in plastic samples, ranging from ~ 2.4 to ~ 120 nm^2/s , with no clear peak value.

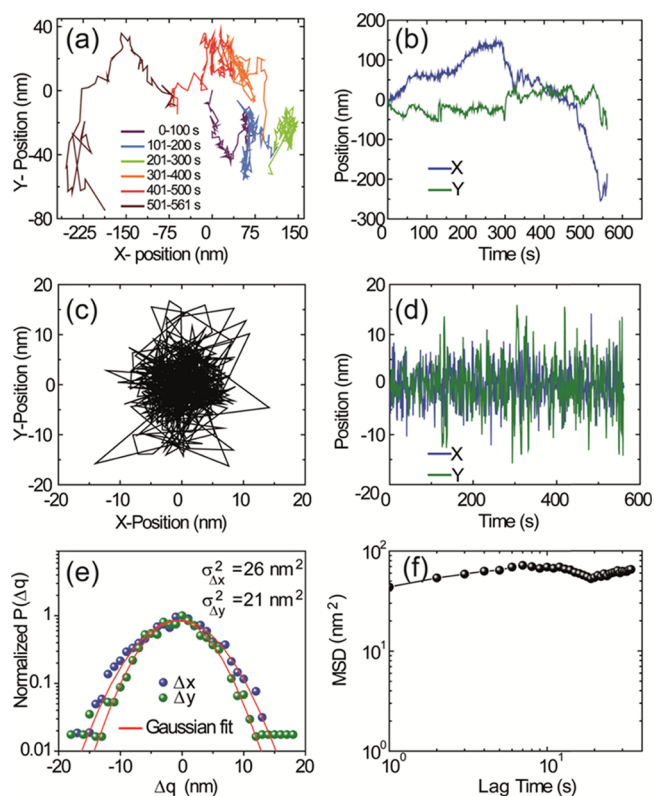


Figure 4. Microscopy investigation of plastic monoliths. (a) Particle trajectory of a single probe particle from fluorescence microscopy. The trajectory is color-coded to show the timescale of motion. (b) Particle motion along X and Y coordinates (defined arbitrarily, as shown in (a)) as a function of time. (c,d) Trajectory and position of a particle after elimination of stage drift using wavelet transform. (e) van Hove jump distribution for a particle along X and Y coordinates and fit to a Gaussian form. (f) MSD for particle movement in the X – Y plane. MSD is calculated and presented as described in the caption for Figure 3.

We examined the MSD (for X and Y) for a large number of probe particles in elastic sponges and plastic monoliths. Consistent with the variation of widths of the jump distributions, we observe that there is a significantly greater nonuniformity in the slopes of the MSD(τ) from probe particles in plastic scaffolds, relative to the elastic ones (Figure 6a,b). At short times (up to 5 s), the MSD is linear in time, which can be used to estimate the 1D diffusivity, D , using the relation: $\text{MSD}(\tau) = 2D\tau$. This corresponds to the diffusive motion of particles over a time of about 5 s. Therefore, this value of diffusivity does not exactly correspond to that obtained from the breadth of the van Hove distribution. However, the range of diffusivity values obtained from the MSD is comparable to that from the van Hove jump distributions as discussed below. This allowed us to construct the distribution of 1D diffusion coefficients (Figure 6c) extracted from all the particles in both elastic scaffold and plastic monoliths. From these distributions, we find that D_{elastic} span from ~ 1.4 to ~ 38 nm^2/s with the most probable value of ≈ 3.5 nm^2/s , whereas the variation of D_{plastic} is much higher and range from ~ 2.1 to ~ 125 nm^2/s with no clear maxima. Thus, the distribution of single-particle diffusivities obtained from MSD(τ) (Figure 6c) for elastic and plastic scaffolds follows the same trend and have similar behaviors as those extracted from the analysis of the van Hove correlation functions (Figure 5c).

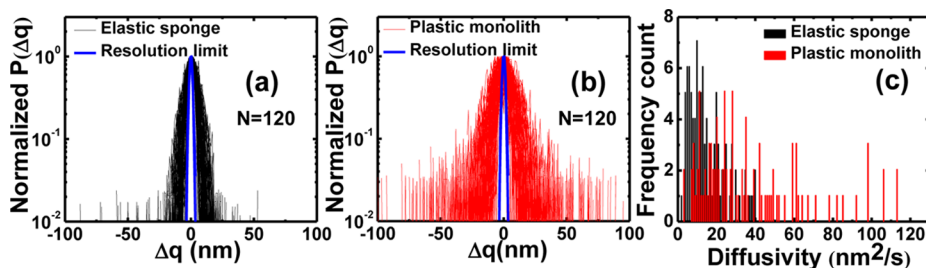


Figure 5. van Hove particle jump distribution for multiple (>100) particles for (a) elastic sponge and (b) plastic monolith. The resolution limit is set by reference glassy matrix and is about ± 2.5 nm. (c) Distribution of particle diffusivity obtained from variance of the jump distribution.

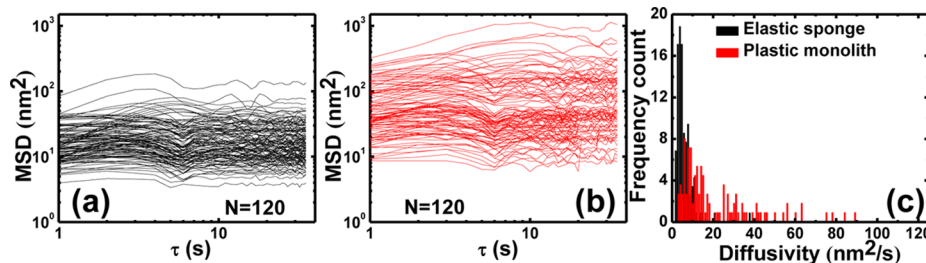


Figure 6. MSD calculated for multiple (>100) particles for (a) elastic sponge and (b) plastic monolith. (c) Distribution of particle diffusivity obtained from the slope of the initial linear regime of MSD.

Using the MSD(τ) data for all the FPS particles, we now calculate local elastic and viscous moduli from the MSD, following Mason (for more details see [Supporting Information S2](#)).⁵⁰ This microrheological method is based on the generalization of the Stokes–Einstein relation to viscoelastic fluids. We observe that the local elastic modulus (G') is frequency-independent for both elastic and plastic scaffolds ([Figure 7a,b](#)). G' calculated from the MSD of probe particles in elastic sponges ranges from 20 to 170 Pa. In comparison, the plastic monoliths exhibit a wider variation in local elastic moduli, ranging from 0.2 to 120 Pa. These differences between the elastic and plastic scaffolds are not readily apparent when we

compare the average value of G' , averaged across all probe particles (compare thick line in [Figure 7a,b](#)). Bulk measurements of the elastic moduli, from dynamic shear rheology on macroscopic samples (lines with symbols in [Figure 7a,b](#)) reveal that the bulk value of G' is comparable for elastic and plastic scaffolds. This is consistent with our observations for the average values of the microscopic G' from microrheology. The values of the bulk elastic moduli are significantly higher than those from microrheological measurements. We discuss possible reasons for this later in the paper. We have also calculated the damping factor ($\tan \delta$) as the ratio of the local viscous modulus (G'') to the elastic modulus (G'). For elastic sponges, $\tan \delta$ varies from 0.04 to 0.2. In comparison, plastic monoliths exhibit a wider range, from 0.04 to 0.5, with most particles showing a $\tan \delta$ between 0.15 and 0.5.

MSD(τ) ([Figure 6a,b](#)) initially increases linearly with time and subsequently plateaus. This is intriguing because the jump distributions follow Gaussian behavior, indicating that the particles are Brownian. Similar observations on anomalous yet Brownian motion of single particles have been reported earlier.^{51,52} We observe that the MSD(τ) saturates over time for all the FPS particles in both elastic and plastic scaffolds ([Figure 6a,b](#)), which is expected because the particles are trapped in a crosslinked polymer mesh that forms a cage, preventing their free diffusion. For all the FPS particles in the elastic scaffold, the MSD plateaus at relatively short lag times of within 6–10 s, whereas for plastic scaffolds, there is a much wider variation in the initiation of MSD saturation timescales of ~ 6 to ~ 30 s.

The particle diffusivity measured using microscopy provides information about the local viscoelastic environment. Variation in the diffusivities reveals spatial differences in this environment in the scaffolds. Further, there are also differences between the time for the MSD to plateau, τ , in elastic and plastic scaffolds. We can estimate the “cage” size that restricts the motion of particles in the scaffold walls as being of the order of $\sqrt{D\tau}$. Thus, in elastic scaffolds we can estimate cage sizes ranging from 2.9 nm (based on a diffusivity of $1.4 \text{ nm}^2/\text{s}$ and $\tau \approx 6$ s) to

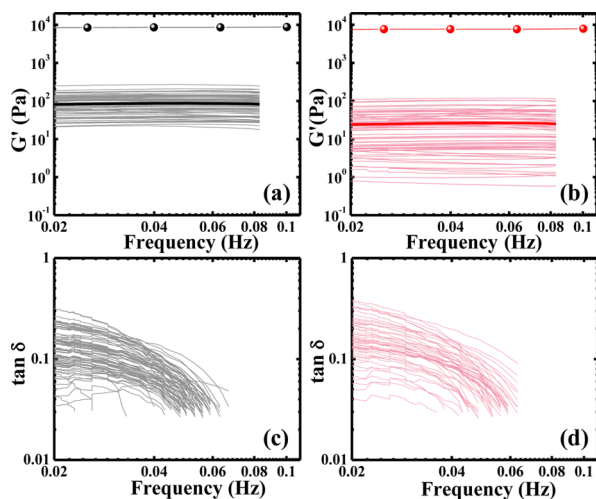


Figure 7. Microrheology and bulk rheology of scaffolds. (a,b) Elastic modulus (G') as a function of frequency obtained for elastic sponge and plastic monolith. The thick solid lines represent average data. Lines with spherical symbols are obtained from bulk dynamic shear rheology measurements, performed in the linear response region, at 0.25% strain. (c,d) The damping coefficient ($\tan \delta$) as a function of frequency calculated for elastic and plastic.

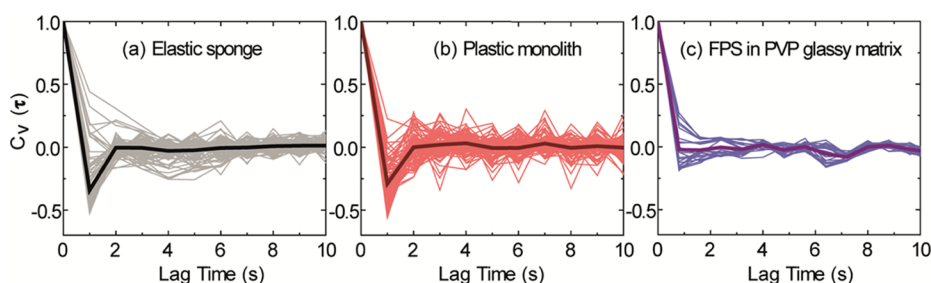


Figure 8. Normalized velocity–velocity autocorrelation function (VACF) plotted for (a) elastic sponge, (b) plastic monolith, and (c) reference sample. VACF of elastic and plastic scaffolds showed sharp negative (or anti) correlations at lag time ≈ 1 s in contrast to the reference glassy sample.

19.5 nm ($D = 38$ nm²/s, $\tau = 10$ s), whereas for the plastic scaffolds, we estimate a wide variation in cage sizes, ranging from 3.5 nm ($D = 2$ nm²/s, $\tau = 6$ s) to 61 nm ($D = 125$ nm²/s, $\tau = 30$ s).

To investigate the origin of subdiffusive behavior exhibited by the FPS in elastic and plastic scaffolds, we analyzed single-particle trajectories to compute the VACF (details are in Supporting Information S2), which can provide insights into tracer movement mechanisms.²⁰ For each particle, the VACF are plotted, as is the average for ease of comparison between the samples (Figure 8). For particles in both elastic and plastic scaffolds (Figure 8a,b), the VACF demonstrates a sharp negative correlation for short times ($\tau = 1$ s), in contrast to the behavior of the reference sample (FPS in glassy polymer matrix, Figure 8c). The negative correlations in the initial time period can arise from two different mechanisms; fractional Brownian motion (FBM) or continuous time random walk (CTRW) in confined systems.⁵³ FBM is essentially associated with the motion of a Brownian particle in a viscoelastic medialike polymer.^{54,55} In a viscoelastic medium, when a Brownian walker takes a step in one direction, the elasticity of the medium results in particle rebound. Therefore, velocities of the particle at successive time instants are negatively correlated at short lag times. CTRW arises when the particle stops intermittently for an interval followed by a movement, leading to a broad waiting time distribution. We do not observe any dwell/pause times during particle motion, suggesting that our data are likely to be more appropriately described using a FBM framework. Further, the difference in behavior between the FPS in ice-templated scaffolds versus in the reference sample confirms that particle motions in the scaffolds obtained from our microscopy data are above the resolution limit of the technique.

Particle tracking microrheology further allows us to estimate local viscoelastic moduli. In contrast to our previously reported macroscopic measurements,¹⁵ there is a difference between the elastic modulus of elastic and plastic scaffolds from microrheology. The values of moduli obtained from microrheology are much lower when compared with bulk rheological measurements. This is not unusual and has been observed for other samples. For example, Caggioni et al. used particle tracking microrheology to study the effect of shear during gelation of aqueous gellan gum with a monovalent salt. They observed that microrheology underestimates the moduli compared to bulk rheology⁵⁴ and attributed this difference to electrostatic repulsion between tracers and the gellan. They suggest that a depletion layer around tracer particles in their work increases their mobility. This has also been suggested by researchers in the context of other biopolymer solutions.⁵⁵ Typically, it is believed that when the length scale character-

izing the sample microstructure is small compared to the tracer dimension, then the microrheology agrees with bulk measurements.^{56,57} If this is not the case, then tracer particle motion is sensitive to local heterogeneities and microrheological results differ from bulk measurements.^{58–60} In our scaffolds, probe particles are integrated into the colloidal assemblies and we do not anticipate that their dynamics will be any different from the matched size silica colloids in the scaffolds.

Bulk rheological measurements show that elastic and plastic monoliths are characterized by similar values of solid modulus, G' and that the loss modulus, G'' , for plastic scaffolds is higher than that for the elastic.¹⁵ The particle tracking measurements reported here reveal a more nuanced description of the assemblies when compared with the bulk measurements. In accord with the bulk measurements, microrheology indicates that the local solid modulus for both scaffolds is greater than the loss modulus. However, both scaffolds show a spatial variation in local values of the solid modulus. This variation is larger for the plastic assemblies relative to the elastic. However, the average values of the solid moduli from microrheological measurements of elastic and plastic assemblies vary only by a factor of about 2, because the average values are strongly weighted by the high modulus regions. Thus, the spatially averaged microrheological solid modulus is comparable for elastic and plastic scaffolds, similar to what is observed from bulk rheological measurements. The solid modulus is proportional to the crosslink density. Therefore, the implication of the microrheology data is that there is a wider variation in crosslink density for the plastic scaffolds relative to the elastic. Remarkably, it appears that this variation is averaged so that the bulk solid moduli (and thus, the average crosslink density) are similar for both scaffolds. Finally, we note that the loss tangent, $\tan \delta (= G''/G')$, that is a measure of energy dissipation, is higher for plastic scaffolds relative to elastic. The variation in $\tan \delta$ too is higher for plastic scaffolds. Thus, consistent with previous AFM measurements,¹⁵ we observe a greater energy dissipation for the plastic scaffolds relative to the elastic assemblies.

The van Hove distribution for particle excursions and the MSD provide information about the dynamical environment experienced by FPS particles in the elastic and plastic scaffolds. Our previous investigations¹⁵ of the static structure of elastic and plastic scaffolds used electron microscopy and small-angle X-ray scattering to probe morphology and nuclear magnetic resonance to probe the chemical composition of these scaffolds. We observed that there were no differences between the morphological structure and average chemical composition of the elastic and plastic scaffolds. However, using AFM to spatially map out the work of adhesion at junctions between particles in scaffold walls, revealed clear differences between the

elastic and plastic scaffolds. We observed that the particle junctions in elastic scaffolds are characterized by the work of adhesion that is narrowly peaked at $\approx 1.5 \text{ J/m}^2$, whereas junctions in plastic scaffolds show a wide range of work of adhesion, up to 11 J/m^2 , without a peak value. We observe a remarkable similarity between this static description of viscoelastic interparticle junctions from AFM and the dynamical motions of the colloidal particles obtained from single-particle tracking measurements. Specifically, differences between the elastic and plastic scaffolds with regard to the distribution of particle diffusivities from MSD data and the variance from the van Hove functions are in remarkable consonance with the AFM work of adhesion. Thus, spatial variation in particle dynamics observed with single-particle tracking is mirrored by the variation in the local viscoelastic properties of the crosslinked polymer matrix reported using AFM. We had previously speculated¹⁵ that the differences between elastic and plastic scaffolds result from variations in the local crosslink density: elastic scaffolds were characterized by a uniform distribution of crosslinks, whereas plastic scaffolds showed a widely heterogeneous crosslink density. Interestingly, our experiments indicate that the length scale that characterizes the heterogeneity in the samples has to be larger than the probe particle size, viz. $1 \mu\text{m}$. We note that this scenario is consistent with the variation in “cage” sizes obtained from particle tracking, for particles in elastic and plastic scaffolds.

4. CONCLUSIONS

We have demonstrated that wavelet transforms can be used to eliminate the effect of stage drift during single-particle tracking microscopy of samples with slow dynamics. We apply this technique to fluorescence microscopy. For samples with high SBRs, eliminating stage drift using wavelet transforms allows us to track particles with a spatial resolution of $\approx 2.5 \text{ nm}$. We note that a high SBR allows us to accurately track the particle positions and is essential to obtain the reported spatial resolution. We investigate ice-templated colloidal assemblies and track the motions of fluorescent particles embedded in these. Variations in the preparation protocol for these colloidal assemblies produce materials that have identical overall chemical composition but dramatically different mechanical response. We track the motion of probe colloidal particles to investigate the local microstructure in elastic assemblies that can recover from large compressive deformations and in plastic assemblies that fail at low strains. Since these assemblies comprise of densely packed colloids that are assembled in a crosslinked polymer mesh, the colloidal motions that we observe are slow and of small amplitude. Therefore, a high SBR in imaging and elimination of stage drift using wavelet transforms is critical to analyzing colloidal dynamics in these samples. The use of wavelet transforms to eliminate stage drift is an enabling technique for high-resolution particle tracking in samples with slow dynamics and might be of wide relevance for microscopic studies of dense colloidal systems. We note that this implementation of wavelet transforms to eliminate stage drift relies on eliminating correlated motions between particles. This assumes that long range, low frequency motions are not correlated over long distances in the sample. While this holds true for a large class of dense soft matter systems,⁶¹ it is not true for dilute colloidal dispersions, where hydrodynamic coupling decays slowly.

There is a significant difference in the MSD of probe particles in elastic and plastic scaffolds, as well as the van Hove

distribution for particle jumps. The variance from the van Hove distribution is peaked around an average value for elastic sponges, in contrast to plastic monoliths that exhibit a wide variation with no clear peak. This trend is mirrored by the particle diffusivities for elastic and plastic scaffolds, calculated from the MSD data. Therefore, we conclude that the key difference between elastic and plastic scaffolds is that plastic scaffolds exhibit large spatial heterogeneity relative to elastic scaffolds. This spatial heterogeneity is manifested in the wide variation in the motion of probe particles at various locations in the plastic scaffolds. We interpret the spatial heterogeneity in the local environment in terms of variations in local crosslink density for plastic scaffolds. This is consistent with micro-rheology data that show greater variation in the local solid moduli for plastic scaffolds than for elastic scaffolds and lower dissipation for elastic assemblies. Thus, particle tracking and microrheology provide a detailed spatial characterization of the local environment in elastic assemblies and plastic monoliths and unambiguously demonstrate the microscopic origin of the differences between them.

■ ASSOCIATED CONTENT

📄 Supporting Information

The Supporting Information is available free of charge on the ACS Publications website at DOI: [10.1021/acs.langmuir.7b04120](https://doi.org/10.1021/acs.langmuir.7b04120).

Correlated motion in reference sample, procedure for particle tracking experiment, image processing and elimination of stage drift using wavelet transform, and correlated motion in elastic sponges (PDF)

■ AUTHOR INFORMATION

Corresponding Authors

*E-mail: arindam@chem.iitb.ac.in. Phone: +91-22-2576-7154 (A.C.).

*E-mail: g.kumaraswamy@ncl.res.in. Phone: +91-20-2590-2182. Fax: +91-20-2590-2618 (G.K.).

ORCID

Karthika Suresh: [0000-0003-4890-2778](https://orcid.org/0000-0003-4890-2778)

Arindam Chowdhury: [0000-0001-8178-1061](https://orcid.org/0000-0001-8178-1061)

Guruswamy Kumaraswamy: [0000-0001-9442-0775](https://orcid.org/0000-0001-9442-0775)

Present Addresses

[†]Ketan Dinkar Sarode, MIT School of Bioengineering Sciences and Research, MIT-ADT University, Pune 412201, Maharashtra, India.

[‡]Dharmendar Kumar Sharma, Department of Materials Science & Engineering, Tokyo Institute of Technology, Ookayama-2-12-1-S8-44, Meguro-ku, Tokyo 152-8552, Japan.

Author Contributions

The work was conceived and supervised by G.K. K.S. performed experiments and analysis. Epifluorescence microscopy was performed with the help from R.C. and D.K.S. Fluorescence microscopy and data analysis were performed under the supervision of A.C. The wavelet analysis was performed with the support of V.R.K. and K.D.S. K.S. and G.K. wrote the manuscript, with inputs from A.C. and V.R.K. All authors have given approval to the final version of the manuscript.

Funding

This work was partially funded by a BRNS grant number 37(3)/14/03/2015-BRNS/10241.

Notes

The authors declare no competing financial interest.

ACKNOWLEDGMENTS

K.S. and D.K.S. thank CSIR and R.C. thanks UGC for the Senior Research Fellowships. A.C. acknowledges IRCC, IIT Bombay for partial financial support. K.S. acknowledges Farsaram for help with the lyophilization technique.

REFERENCES

- (1) Sun, B.; Sirringhaus, H. Solution-processed zinc oxide field-effect transistors based on self-assembly of colloidal nanorods. *Nano Lett.* **2005**, *5*, 2408–2413.
- (2) Li, F.; Josephson, D. P.; Stein, A. Colloidal Assembly: The Road from Particles to Colloidal Molecules and Crystals. *Angew. Chem., Int. Ed.* **2011**, *50*, 360–388.
- (3) Ozin, G. A.; Hou, K.; Lotsch, B. V.; Cademartiri, L.; Puzzo, D. P.; Scotognella, F.; Ghadimi, A.; Thomson, J. Nanofabrication by self-assembly. *Mater. Today* **2009**, *12*, 12–23.
- (4) Panyam, J.; Labhasetwar, V. Biodegradable nanoparticles for drug and gene delivery to cells and tissue. *Adv. Drug Delivery Rev.* **2003**, *55*, 329–347.
- (5) Yager, P.; Edwards, T.; Fu, E.; Helton, K.; Nelson, K.; Tam, M. R.; Weigl, B. H. Microfluidic diagnostic technologies for global public health. *Nature* **2006**, *442*, 412.
- (6) Lewis, L. N. Chemical catalysis by colloids and clusters. *Chem. Rev.* **1993**, *93*, 2693–2730.
- (7) Pierre, A. C.; Pajonk, G. M. Chemistry of aerogels and their applications. *Chem. Rev.* **2002**, *102*, 4243–4266.
- (8) Wang, J.; Cheng, Q.; Tang, Z. Layered nanocomposites inspired by the structure and mechanical properties of nacre. *Chem. Soc. Rev.* **2012**, *41*, 1111–1129.
- (9) Jang, D.; Meza, L. R.; Greer, F.; Greer, J. R. Fabrication and deformation of three-dimensional hollow ceramic nanostructures. *Nat. Mater.* **2013**, *12*, 893–898.
- (10) Zheng, X.; Lee, H.; Weisgraber, T. H.; Shusteff, M.; DeOtte, J.; Duoss, E. B.; Kuntz, J. D.; Biener, M. M.; Ge, Q.; Jackson, J. A. Ultralight, ultrastiff mechanical metamaterials. *Science* **2014**, *344*, 1373–1377.
- (11) Lee, L.; Zeng, C.; Cao, X.; Han, X.; Shen, J.; Xu, G. Polymer nanocomposite foams. *Compos. Sci. Technol.* **2005**, *65*, 2344–2363.
- (12) Rajamanickam, R.; Kumari, S.; Kumar, D.; Ghosh, S.; Kim, J. C.; Tae, G.; Gupta, S. S.; Kumaraswamy, G. Soft colloidal scaffolds capable of elastic recovery after large compressive strains. *Chem. Mater.* **2014**, *26*, 5161–5168.
- (13) Das, C.; Chatterjee, S.; Kumaraswamy, G.; Krishnamoorthy, K. Elastic Compressible Energy Storage Devices from Ice Templated Polymer Gels treated with Polyphenols. *J. Phys. Chem. C* **2017**, *121*, 3270–3278.
- (14) Chatterjee, S.; Gupta, S. S.; Kumaraswamy, G. Omniphilic Polymeric Sponges by Ice Templating. *Chem. Mater.* **2016**, *28*, 1823–1831.
- (15) Suresh, K.; Patil, S.; Rajamohanam, P. R.; Kumaraswamy, G. The Template Determines Whether Chemically Identical Nanoparticle Scaffolds Show Elastic Recovery or Plastic Failure. *Langmuir* **2016**, *32*, 11623–11630.
- (16) Weeks, E. R.; Weitz, D. A. Subdiffusion and the cage effect studied near the colloidal glass transition. *Chem. Phys.* **2002**, *284*, 361–367.
- (17) Cheng, X.; McCoy, J. H.; Israelachvili, J. N.; Cohen, I. Imaging the microscopic structure of shear thinning and thickening colloidal suspensions. *Science* **2011**, *333*, 1276–1279.
- (18) Ruthardt, N.; Lamb, D. C.; Bräuchle, C. Single-particle tracking as a quantitative microscopy-based approach to unravel cell entry mechanisms of viruses and pharmaceutical nanoparticles. *Mol. Ther.* **2011**, *19*, 1199–1211.
- (19) Meijering, E.; Dzyubachyk, O.; Smal, I.; van Cappellen, W. A. Tracking in cell and developmental biology. *Seminars in Cell & Developmental Biology*; Elsevier, 2009; pp 894–902.
- (20) Bhattacharya, S.; Sharma, D. K.; Saurabh, S.; De, S.; Sain, A.; Nandi, A.; Chowdhury, A. Plasticization of poly (vinylpyrrolidone) thin films under ambient humidity: Insight from single-molecule tracer diffusion dynamics. *J. Phys. Chem. B* **2013**, *117*, 7771–7782.
- (21) Shen, H.; Tauzin, L. J.; Baiyasi, R.; Wang, W.; Moringo, N.; Shuang, B.; Landes, C. F. Single Particle Tracking: From Theory to Biophysical Applications. *Chem. Rev.* **2017**, *117*, 7331–7376.
- (22) Saxton, M. J.; Jacobson, K. Single-particle tracking: applications to membrane dynamics. *Annu. Rev. Biophys. Biomol. Struct.* **1997**, *26*, 373–399.
- (23) Valentine, M. T.; Kaplan, P. D.; Thota, D.; Crocker, J. C.; Gisler, T.; Prud'homme, R. K.; Beck, M.; Weitz, D. A. Investigating the microenvironments of inhomogeneous soft materials with multiple particle tracking. *Phys. Rev. E: Stat., Nonlinear, Soft Matter Phys.* **2001**, *64*, 061506.
- (24) Mason, T. G.; Ganesan, K.; Van Zanten, J. H.; Wirtz, D.; Kuo, S. C. Particle tracking microrheology of complex fluids. *Phys. Rev. Lett.* **1997**, *79*, 3282.
- (25) Anthony, S. M.; Hong, L.; Kim, M.; Granick, S. Single-particle colloid tracking in four dimensions. *Langmuir* **2006**, *22*, 9812–9815.
- (26) Kegel, W. K.; van Blaaderen, A. Direct Observation of Dynamical Heterogeneities in Colloidal Hard-Sphere Suspensions. *Science* **2000**, *287*, 290–293.
- (27) Mortensen, K. I.; Churchman, L. S.; Spudich, J. A.; Flyvbjerg, H. Optimized localization analysis for single-molecule tracking and super-resolution microscopy. *Nat. Methods* **2010**, *7*, 377–381.
- (28) Biteen, J.; Willems, K. A. Introduction: Super-Resolution and Single-Molecule Imaging. *Chem. Rev.* **2017**, *117*, 7241–7243.
- (29) Axelrod, D. Total internal reflection fluorescence microscopy in cell biology. *Traffic* **2001**, *2*, 764–774.
- (30) van Loenhout, M. T. J.; Kerssemakers, J. W. J.; De Vlamincq, I.; Dekker, C. Non-bias-limited tracking of spherical particles, enabling nanometer resolution at low magnification. *Biophys. J.* **2012**, *102*, 2362–2371.
- (31) Adler, J.; Pagakis, S. N. Reducing image distortions due to temperature-related microscope stage drift. *J. Microsc.* **2003**, *210*, 131–137.
- (32) Thompson, R. E.; Larson, D. R.; Webb, W. W. Precise nanometer localization analysis for individual fluorescent probes. *Biophys. J.* **2002**, *82*, 2775–2783.
- (33) Lee, S. H.; Baday, M.; Tjioe, M.; Simonson, P. D.; Zhang, R.; Cai, E.; Selvin, P. R. Using fixed fiducial markers for stage drift correction. *Opt. Express* **2012**, *20*, 12177–12183.
- (34) Brunelli, R. *Template Matching Techniques in Computer Vision: Theory and Practice*; John Wiley & Sons, 2009.
- (35) Bloëß, A.; Durand, Y.; Matsushita, M.; Van Dermeer, H.; Brakenhoff, G. J.; Schmidt, J. Optical far-field microscopy of single molecules with 3.4 nm lateral resolution. *J. Microsc.* **2002**, *205*, 76–85.
- (36) Carter, A. R.; King, G. M.; Ulrich, T. A.; Halsey, W.; Alchenberger, D.; Perkins, T. T. Stabilization of an optical microscope to 0.1 nm in three dimensions. *Appl. Opt.* **2007**, *46*, 421–427.
- (37) Crocker, J. C.; Hoffman, B. D. Multiple particle tracking and two point microrheology in cells. *Methods Cell Biol.* **2007**, *83*, 141–178.
- (38) Crocker, J. C.; Valentine, M. T.; Weeks, E. R.; Gisler, T.; Kaplan, P. D.; Yodh, A. G.; Weitz, D. A. Two-point microrheology of inhomogeneous soft materials. *Phys. Rev. Lett.* **2000**, *85*, 888.
- (39) Unser, M. Wavelets: on the virtues and applications of the mathematical microscope. *J. Microsc.* **2014**, *255*, 123–127.
- (40) Strang, G.; Nguyen, T. *Wavelets and Filter Banks*; SIAM, 1996.
- (41) Strang, G. Wavelet transforms versus Fourier transforms. *Bull. Am. Math. Soc.* **1993**, *28*, 288–305.
- (42) Polikar, R. *The Wavelet Tutorial*, 1996.
- (43) Rioul, O.; Vetterli, M. Wavelets and signal processing. *IEEE Signal Process. Mag.* **1991**, *8*, 14–38.

- (44) Jensen, A.; la Cour-Harbo, A. *Ripples in Mathematics: The Discrete Wavelet Transform*; Springer Science & Business Media, 2001.
- (45) Roy, M.; Kumar, V. R.; Kulkarni, B. D.; Sanderson, J.; Rhodes, M.; vander Stappen, M. Simple denoising algorithm using wavelet transform. *AIChE J.* **1999**, *45*, 2461–2466.
- (46) Kulkarni, A. A.; Joshi, J. B.; Kumar, V. R.; Kulkarni, B. D. Wavelet transform of velocity-time data for the analysis of turbulent structures in a bubble column. *Chem. Eng. Sci.* **2001**, *56*, 5305–5315.
- (47) Deshpande, S. S.; Tabib, M. V.; Joshi, J. B.; Kumar, V. R.; Kulkarni, B. D. Analysis of flow structures and energy spectra in chemical process equipment. *J. Turbul.* **2010**, *11*, N5.
- (48) Kumar, V. R.; Kulkarni, B. D.; Dixit, N. M.; Vaish, N. Method and an apparatus for the identification and/or separation of complex composite signals into its deterministic and noisy components. U.S. Patent 6,208,951, 2001.
- (49) Hopkins, P.; Fortini, A.; Archer, A. J.; Schmidt, M. The van Hove distribution function for Brownian hard spheres: Dynamical test particle theory and computer simulations for bulk dynamics. *J. Chem. Phys.* **2010**, *133*, 224505.
- (50) Mason, T. G. Estimating the viscoelastic moduli of complex fluids using the generalized Stokes-Einstein equation. *Rheol. Acta* **2000**, *39*, 371–378.
- (51) Wang, B.; Kuo, J.; Bae, S. C.; Granick, S. When Brownian diffusion is not Gaussian. *Nat. Mater.* **2012**, *11*, 481–485.
- (52) Bronstein, I.; Israel, Y.; Kepten, E.; Mai, S.; Shav-Tal, Y.; Barkai, E.; Garini, Y. Transient anomalous diffusion of telomeres in the nucleus of mammalian cells. *Phys. Rev. Lett.* **2009**, *103*, 018102.
- (53) Magdziarz, M.; Weron, A.; Burnecki, K.; Klafter, J. Fractional Brownian motion versus the continuous-time random walk: A simple test for subdiffusive dynamics. *Phys. Rev. Lett.* **2009**, *103*, 180602.
- (54) Caggioni, M.; Spicer, P. T.; Blair, D. L.; Lindberg, S. E.; Weitz, D. A. Rheology and microrheology of a microstructured fluid: The gellan gum case. *J. Rheol.* **2007**, *51*, 851–865.
- (55) Liu, J.; Gardel, M. L.; Kroy, K.; Frey, E.; Hoffman, B. D.; Crocker, J. C.; Bausch, A. R.; Weitz, D. A. Microrheology probes length scale dependent rheology. *Phys. Rev. Lett.* **2006**, *96*, 118104.
- (56) Dasgupta, B. R.; Tee, S.-Y.; Crocker, J. C.; Frisken, B. J.; Weitz, D. A. Microrheology of polyethylene oxide using diffusing wave spectroscopy and single scattering. *Phys. Rev. E: Stat., Nonlinear, Soft Matter Phys.* **2002**, *65*, 051505.
- (57) Mason, T. G.; Weitz, D. A. Optical measurements of frequency-dependent linear viscoelastic moduli of complex fluids. *Phys. Rev. Lett.* **1995**, *74*, 1250.
- (58) Wong, I. Y.; Gardel, M. L.; Reichman, D. R.; Weeks, E. R.; Valentine, M. T.; Bausch, A. R.; Weitz, D. A. Anomalous diffusion probes microstructure dynamics of entangled F-actin networks. *Phys. Rev. Lett.* **2004**, *92*, 178101.
- (59) Palmer, A.; Mason, T. G.; Xu, J.; Kuo, S. C.; Wirtz, D. Diffusing wave spectroscopy microrheology of actin filament networks. *Biophys. J.* **1999**, *76*, 1063–1071.
- (60) Gardel, M. L.; Valentine, M. T.; Crocker, J. C.; Bausch, A. R.; Weitz, D. A. Microrheology of entangled F-actin solutions. *Phys. Rev. Lett.* **2003**, *91*, 158302.
- (61) Crocker, J. C.; Valentine, M. T.; Weeks, E. R.; Gisler, T.; Kaplan, P. D.; Yodh, A. G.; Weitz, D. A. Two-point microrheology of inhomogeneous soft materials. *Phys. Rev. Lett.* **2000**, *85*, 888.